On the Efficacy of Compact Radar Transponders for InSAR Geodesy: Results of Multiyear Field Tests

Richard Czikhardt, Hans van der Marel, Juraj Papco, and Ramon F. Hanssen, *Senior Member, IEEE*

Abstract—Compact and low-cost radar transponders are an attractive alternative to corner reflectors (CRs) for interferometric synthetic aperture radar (InSAR) deformation monitoring, datum connection, and geodetic data integration. Recently, such transponders have become commercially available for C-band sensors, which poses relevant questions on their characteristics in terms of radiometric, geometric, and phase stability. Especially for extended time series and for high-precision geodetic applications, the impact of secular or seasonal effects, such as variations in temperature and humidity, has yet to be proven. In this article, we address these challenges using a multitude of short baseline experiments with four transponders and six CRs deployed at test sites in The Netherlands and Slovakia. Combined together, we analyzed 980 transponder measurements in Sentinel-1 time series to a maximum extent of 21 months. We find an average radar cross section (RCS) of over 42 dBm^2 within a range of up to 15° of elevation misalignment, which is comparable to a triangular trihedral CR with a leg length of 2.0 m. Its RCS shows the temporal variations of 0.3–0.7 dBm^2 (standard deviation), which is partially correlated with surface temperature changes. The precision of the InSAR phase double differences over short baselines between a transponder and a stable reference CRs is found to be 0.5–1.2 mm (one sigma). We observe a correlation with surface temperature, leading to seasonal variations of up to ±3 mm, which should be modeled and corrected for in high-precision InSAR applications. For precise SAR positioning, we observe antenna-specific constant internal electronic delays of 1.2–2.1 m in slant range, i.e., within the range resolution of the Sentinel-1 interferometric wide (IW) product, with a temporal variability of less than 20 cm. Comparing similar transponders from the same series, we observe distinct differences in performance. Our main conclusion is that these characteristics are favorable for a wide range of geodetic applications. For particular demanding applications, individual calibration of single devices is strongly recommended.

Index Terms—C-band, compact radar transponders, corner reflector (CR), radar-cross-section (RCS), SAR positioning, synthetic aperture radar (SAR), synthetic aperture radar interferometry (InSAR), transponders.

I. INTRODUCTION

RADAR transponders are active electronic devices that receive a radar signal, amplify it, and transmit it back to its source, such as a satellite carrying a synthetic aperture radar (SAR) antenna. They can serve as a compact alternative

Richard Czikhardt and Juraj Papco are with the Department of Theoretical Geodesy and Geoinformatics, Slovak University of Technology, 810 05 Bratislava, Slovakia (e-mail: richard.czikhardt@stuba.sk).

Hans van der Marel and Ramon F. Hanssen are with the Department of Geoscience and Remote Sensing, Delft University of Technology, 2628 CN Delft, The Netherlands.

to corner reflectors (CRs) for precise SAR positioning [1], [2], interferometric synthetic aperture radar (InSAR), deformation monitoring over areas with few natural coherent scatterers [3], InSAR datum connection, and geodetic data integration to provide an absolute reference to the inherently relative InSAR measurements [4].

Recently, medium-to-low-cost transponders for such applications have entered the market for C-band SAR sensors, which triggers questions about their performance and applicability for specific studies. In particular, this concerns their precise radiometric and geometric characteristics, InSAR phase stability, and dependence of external secular or seasonal effects, such as variations in temperature and humidity. Especially for long-term geodetic applications or as permanent reference stations, there is a need for performance metrics. The aim of this study is to derive these quantitative quality metrics based on multiyear experiments with transponders.

II. RADAR TRANSPONDERS

We used C-band transponders manufactured in [5], locally referred to as electronic corner reflectors (ECRs), see Fig. 1. Measuring 360 × 570 × 233 mm, they contain two pairs of transmit and receive antennas for the ascending and descending orbits of SAR satellites, such as Sentinel-1 and Radarsat-2. The distance between the receive and transmit antennas is 450 mm to avoid interference. The transponder receives the C-band signal via a squinted receive "patch" antenna, amplifies it, and transmits it back to the source using an equally oriented transmit "patch" antenna. It operates at a bandwidth of 5.405 GHz ± 100 MHz. The antennas are placed under the protective plastic dome, see Fig. 1(a), transparent to C-band signals. Their orientation can be optimized for the average line-of-sight (LOS) direction at the latitude at which they are deployed. For European latitudes, they are squinted in azimuth by 12° (southward from the east–west direction) and tilted in elevation by 32° with respect to the zenith. The azimuth and elevation beamwidths are 20° and 40°, respectively, enabling an orientation to the average Sentinel-1 incidence and zero-Doppler angles for overlapping tracks, while allowing for slight misalignment. The transponder can be configured to receive and transmit in either vertical or horizontal linear polarization and is switched ON automatically based on the selected satellite overpass times. The main function of the integrated GNSS receiver, with 22 tracking channels, is to keep the internal clock synchronized with respect to the
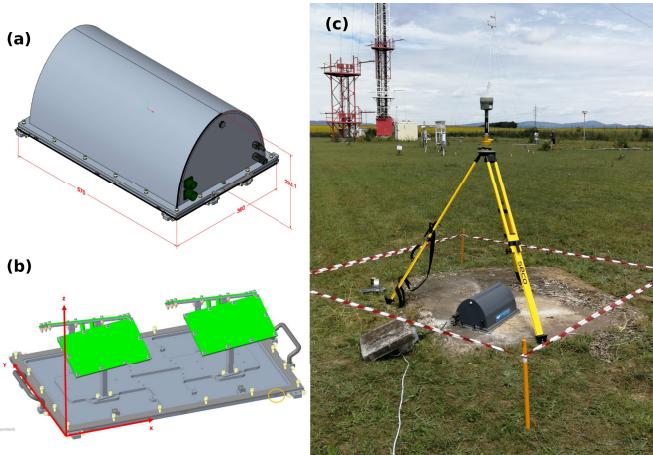
Fig. 1. (a) ECR-C model. (b) Antennas under radome [5]. (c) ECR141 during static GNSS positioning.

time reference (UTC). The time of synchronization can be programmed on a regular basis, e.g., every 12 h.

The theoretical radar cross section (RCS) of the transponder can be determined from the gains of its components [6], [7]

$$\text{RCS} = G_{\text{RF}} \frac{G_{\text{tx}} G_{\text{rx}}}{4\pi} \lambda^2 \qquad (1)$$

where G_{RF} is the gain of the RF amplifying section, G_{tx} and G_{rx} are the gains of the transmit and receive antennas, respectively, and λ is the received signal's wavelength. For our devices, the same patch antenna types are used for receive/transmit, as well as for ascending/descending orientation, with a gain of 15 dBi. The RF chain consists of three amplifiers and a pair of bandpass filters before and after each amplifier to avoid interference from other devices. With an expected overall RF gain of 50 dB, the expected RCS of the transponders is 44 dBm^2. The characteristics of the used transponders are summarized in Table I.

III. Experiment Setup

Four transponders, located at test site JABO in Slovakia and WASS in The Netherlands, are evaluated in experiments covering nearly 1000 SAR interferometric wide (IW) swath acquisitions of the Sentinel-1 satellites. Here, we discuss the two test sites and the characteristics of the time series.

A. Test Site JABO, Slovakia

Transponder units 141 and 148 were installed at July 9, 2020 at a meteorological station near the permanent GNSS station JABO of the SKPOS network in Slovakia (see Fig. 2). The distance between the two units is 46.5 m, which is ideal for the double-difference (DD) InSAR phase observations. The transponders are fastened on horizontal (leveled) concrete slabs. Assuming ascending and descending antenna symmetry, both units were precisely oriented with respect to the north of the conventional terrestrial reference frame (CTRF) [8], with the help of two points staked out using real-time kinematic (RTK) GNSS receivers connected to SKPOS service. The position of the transponders is selected such that it guarantees a high signal-to-clutter ratio (SCR). This is

TABLE I
TRANSPONDER CHARACTERISTICS AS SPECIFIED IN [5]

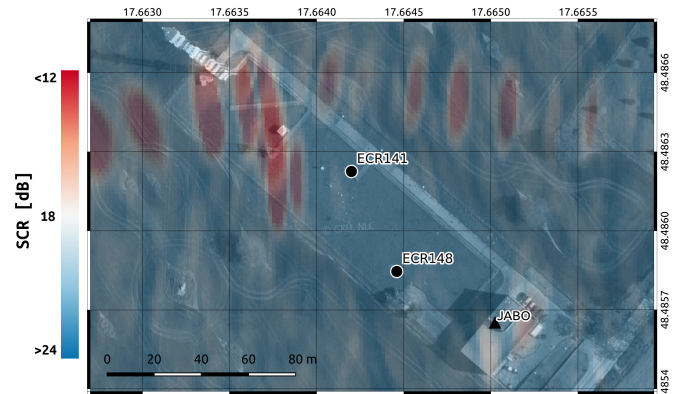|	
Size	$360 \times 570 \times 233$ mm
Bandwidth	100 MHz (5405 $\pm$ 50 MHz)
Antennas	$2 \times$ (Rx + Tx) ascending/descending
Antenna polarization	H/V (only one at time)
Antenna gain	15 dBi
Antenna beamwidth	40° (elevation), 20° (azimuth)
Antenna orientation	32° (elevation tilt), 12° (azimuth squint)
RF gain	50 dB
Expected RCS	44.0 dBm^2
Expected electrical delay	10 ns (1.5 m)

Fig. 2. Experiment setup with transponders 141 and 148 at the JABO meteorological station, Slovakia. The base layer contains the simulated SCR superimposed on a grayscale orthomosaic [9].

attained by estimating the site's clutter power from one year of Sentinel-1 time series prior to deployment and conservatively assuming a transponder RCS of 30 dBm^2, equivalent to a 1-m leg-length triangular trihedral CR. The resultant simulated SCR is superimposed on the orthomosaic in Fig. 2. To avoid interference of impulse response of the two transponders, they are separated from nearby point scatterers by at least two resolution cells in range ($\sim$6 m) and azimuth direction ($\sim$42 m) for both ascending and descending Sentinel-1 tracks.

Both transponders are programmed to receive and transmit in the VV polarization for all regular Sentinel-1 acquisitions over the JABO station (see Table II). They are activated 4 min prior to the satellite overpass to warm up the RF chain and to stabilize the phase response and deactivated 2 min afterward. GNSS time synchronization is scheduled each day at 12 A.M. such that it does not interfere with the planned activations.

B. Test Site WASS, The Netherlands

The second experiment is performed at the TU Delft geodetic test site, WASS, located in Wassenaar, The Netherlands (see Fig. 3). We test the performance of transponder 100, an initial series unit covering a 21-month time series, and transponder 128, which was manufactured in the same series as units 141 and 148 used in Slovakia. Apart from the transponders, the WASS test site includes six passive CRs on a stable foundation. Two large square-based trihedral reflectors with an inner edge length of 1.425 m and a corresponding peak-RCS of 40.7 dBm^2 (C-band) are referred to as CRAS and CRDS
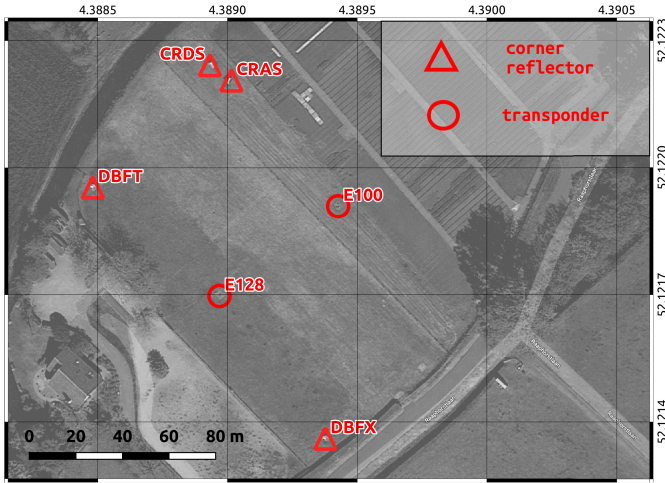
Fig. 3. Wassenaar test site, The Netherlands: experiment setup with transponders 100 and 128 and reference CRs CRAS, CRDS, DBFT, and DBFX.

TABLE II

SENTINEL-1 ACQUISITION TIMES SCHEDULED FOR TRANSPONDERS 141 AND 148 AT THE JABO TEST SITE. THE SUFFIX BEHIND THE TRACK NUMBER INDICATES THE ASCENDING AND DESCENDING ORBIT DIRECTION

Track	UTC	incidence angle	zero-Doppler direction
124d	05:02	37.14°	100.32°
051d	04:54	45.60°	98.79°
073a	16:43	41.78°	260.48°
175a	16:35	32.48°	258.93°

for the ascending and descending orbit orientations, respectively. Two integrated geodetic reference stations (IGRSs) [10] both contain double (ascending and descending) back-flipped triangular trihedral reflectors. The first, referred to as DBFT, has an inner edge length of 0.9 m and a corresponding peak-RCS of 29.5 dBm^2 (C-band), while the second, DBFX, has an effective edge length of 1.36 m and a corresponding peak-RCS of 36.7 dBm^2 (C-band). All these reference reflectors are deployed since 2017 and their RCS and phase stability are well known. Transponders 100 and 128 form very short baselines with respect to these reference reflectors and are scheduled for all regular Sentinel-1 acquisition times (see Table III). The long-term stability of the concrete slabs carrying the transponders has been verified by repeated leveling measurements, surveyed since 2013. To analyze the influence of external conditions on the transponder measurements, we use meteorological data from the KNMI station Voorschoten, at a distance of 4 km from the test site WASS.

C. Sentinel-1 Time Series Analysis

The radiometric, interferometric, and positioning performance of the four transponders is analyzed using Sentinel-1 SLC time series acquired from two overlapping ascending and two overlapping descending tracks. Table IV summarizes the number of Sentinel-1 data used for the operational period of the tested transponders. The effective acquisition interval for

TABLE III

SENTINEL-1 ACQUISITION TIMES SCHEDULED FOR TRANSPONDERS 100 AND 128 AT THE WASS TEST SITE. THE SUFFIX BEHIND THE TRACK NUMBER INDICATES THE ASCENDING AND DESCENDING ORBIT DIRECTION

Track	UTC	incidence angle	zero-Doppler direction
110d	05:58	36.69°	100.54°
037d	05:50	44.65°	98.92°
161a	17:33	41.76°	260.46°
088a	17:25	33.24°	258.83°

the two Sentinel-1 satellites is six days. Due to the chosen settings of the transponders, only data in VV polarization are used for the analysis.

The SAR time series analysis of the transponders is performed using the open-source toolbox GECORIS [11]. For the position of each transponder in each of the SLCs, an image patch of 10 × 10 resolution cells is selected and oversampled by a factor 32 in the frequency domain by zero padding. Then, we estimate the precise peak position and amplitude by fitting a 2-D elliptic paraboloid over a small image subpatch, centered at the oversampled amplitude maximum of the initial patch. This procedure guarantees a peak detection precision of better than 1/100 pixel [12]–[14], which is equivalent to an uncertainty of <2 and <13 cm in the range and azimuth directions of the Sentinel-1 SLC products, respectively.

IV. RESULTS

In the following, we discuss the results of our experiments considering the amplitude behavior, InSAR phase stability, and absolute positioning in Sections IV-A–IV-C, respectively.

A. Radiometry

A transponder approximates an ideal radar point scatterer with a 2-D sinc-like impulse response function (IRF). The instantaneous RCS of a transponder, per acquisition, is estimated using the peak method [15], [16]

$$\text{RCS} = \bar{\beta}_0 \cdot \Delta_{\text{az}} \cdot \Delta_r \quad \left[\text{m}^2\right] \tag{2}$$

where $\bar{\beta}_0$ is the peak radar brightness obtained from the precisely estimated peak amplitude via the pixel scaling factor [17], and $\Delta_{\text{az}}/\Delta_r$ are the azimuth and range resolution, respectively. The peak radar brightness, $\bar{\beta}_0$, is corrected for the noise-equivalent sigma zero (NESZ) [18] and the clutter power. For our test sites, we estimate the clutter power from the Sentinel-1 SAR time series prior to the installation of the transponders, which is demonstrated to be −9 dB on average and temporally stationary by [19].

Fig. 4 shows an example of the radar brightness for the two transponders at the JABO test site. The RCS time series of these two transponders, including the three months of clutter observed before their deployment, are shown in Fig. 5. The outliers for unit 148 in July 2020 are the consequence of a firmware problem, causing the unit not to switch on during these satellite overpasses. These outliers were removed

TABLE IV
SUMMARY OF THE FOUR TESTED TRANSPONDERS AND SENTINEL-1 DATA USED UNTIL MARCH 28, 2021

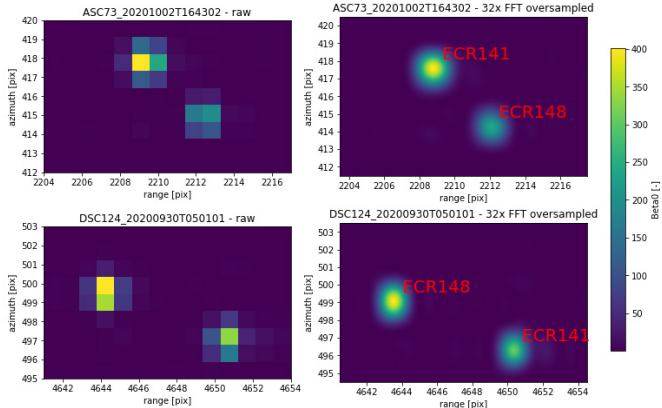| Transponder	Location	Operational since	No. Sentinel-1A+B acquisitions	
			ascending	descending
100	WASS, Wassenaar, Netherlands	2019-06-19	104 + 105	107 + 106
128	WASS, Wassenaar, Netherlands	2020-04-04	56 + 58	58 + 58
141	JABO, Jaslovske Bohunice, Slovakia	2020-07-09	41 + 42	41 + 40
148	JABO, Jaslovske Bohunice, Slovakia	2020-07-09	41 + 42	41 + 40

Fig. 4. Radar brightness β_0 image patch showing two transponders (units 141 and 148) at the JABO test site, from ascending track 73 (top row) and descending track 124 (bottom row) for a single acquisition. (Left) Raw data. (Right) Oversampled data, factor 32.
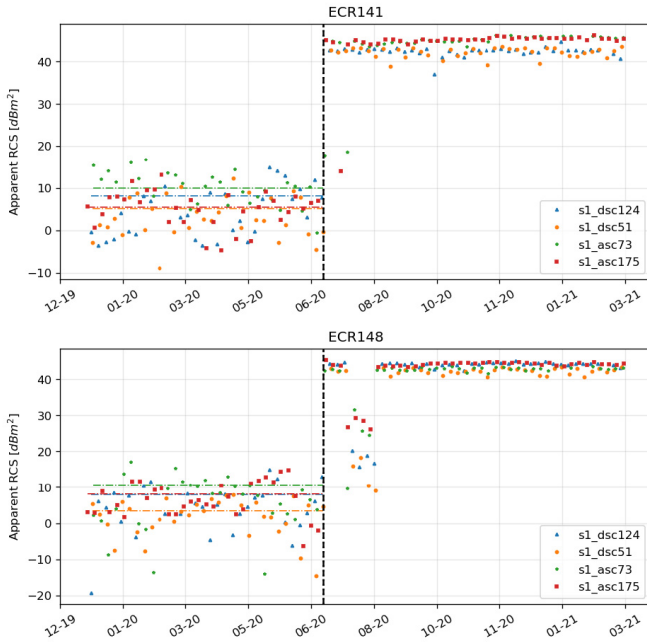

Fig. 5. RCS time series of transponders 141 and 148 at the JABO test site for the four Sentinel-1 tracks. The dashed vertical line represents the installation time.

from the time series analysis using the three median absolute deviation (MAD) criteria [20].

Fig. 6 shows an example of the oversampled radar brightness for all reflectors at the WASS test site.

The RCS time series statistics for all four transponders are summarized in Table V. The temporal average RCS of the
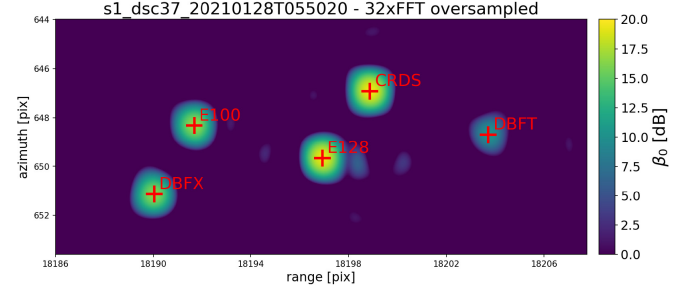

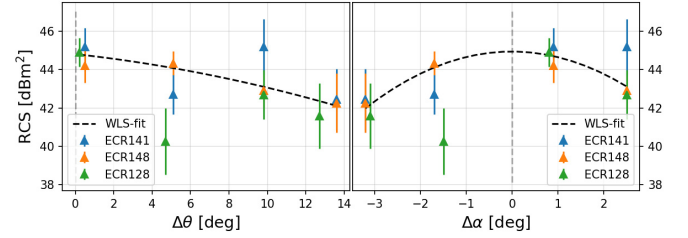Fig. 6. Radar brightness β_0 image patch showing all reflectors at the WASS test site.

Fig. 7. RCS versus antenna misalignment in elevation ($\Delta\theta$) and azimuth ($\Delta\alpha$) angles. A WLS fit approximates the attenuation by a quadratic polynomial. Error bars are 2.5σ.

units 128, 141, and 148 ranges from 42 to 45 dBm^2 across Sentinel-1 tracks, whereas the temporal average RCS of unit 100, which is an older prototype, is approximately 4 dB lower. Note that 45 dBm^2 is equivalent to a triangular trihedral CR with a leg length longer than 2.0 m. These values are in agreement with the theoretical value computed using (1).

1) Alignment Sensitivity: Table V shows that the RCS averages differ between tracks, depending on incidence angle and zero-Doppler direction (see Tables II and III), resulting in antenna misalignment and subsequently RCS attenuation. The misalignment in the elevation ($\Delta\theta$) is computed as the acquisition's incidence angle minus the antenna's elevation tilt (32°) and the misalignment in the azimuth ($\Delta\alpha$) is computed as the acquisition's zero-Doppler angle minus 90° minus the antenna's azimuth squint (12°). Fig. 7 shows this average RCS plotted against a misalignment in elevation and azimuth angles. We observe maximally 3-dB RCS loss for 13° and −3° misalignment in elevation and azimuth angles, respectively. Compared to a triangular trihedral CR, an equivalent misalignment would yield an attenuation of ∼1.5 dB. Considering an SCR of 20 dB, a 3-dB loss increases the phase error by ∼0.1 mm [19], [21]. We approximate the observed attenuation by a quadratic polynomial via a weighted-least-squares (WLS) fit (excluding the data from prototype transponder 100 due

TABLE V
RADIOMETRIC STATISTICS OF THE FOUR TRANSPONDERS ON FOUR INDEPENDENT SENTINEL-1 TIME SERIES

Transponder	No. acquisitions	Track	Misalignment [deg]		RCS [dBm^2]		Avg. SCR [dB]
			Δelevation	Δazimuth	mean	std	
100	107	37d	4.7	−1.5	37.25	.58	28.65
	106	110d	12.7	−3.1	38.41	.68	29.41
	104	161a	9.8	2.5	37.74	.46	29.24
	105	88a	.2	.8	40.30	.46	33.40
128	58	37d	4.7	−1.5	40.26	.69	31.66
	58	110d	12.7	−3.1	41.59	.68	32.59
	56	161d	9.8	2.5	42.69	.51	34.19
	58	88a	.2	.8	44.90	.30	38.00
141	41	124d	5.1	−1.7	42.71	.42	34.55
	40	51d	13.6	−3.2	42.45	.63	37.38
	41	73a	9.8	2.5	45.19	.58	35.20
	42	175a	.5	.9	45.18	.40	39.75
148	37	124d	5.1	−1.7	42.71	.42	34.55
	36	51d	13.6	−3.2	42.26	.62	36.85
	37	73a	9.8	2.5	42.90	.35	32.46
	38	175a	.5	.9	44.22	.36	36.09

to its constant offset). The only large residual appears for unit 128, track 37, which may be due to a slightly erroneous antenna orientation within the sealed casing of the transponder. The 4-dB loss would equal approximately 20° misalignment in elevation or 5° misalignment in azimuth considering our fits. The azimuth misalignment is more likely.

2) Temporal Stability: Comparing the temporal RCS stability of the transponders with conventional CRs, see Table VI, we find that despite the higher average RCS of the transponders, their RCS standard deviations (STDs), σ_{RCS}, are significantly higher. For the WASS test site, both the reflectors and the transponders experience identical clutter conditions, which implies that the observed σ_{RCS} is not influenced by the clutter. In fact, the temporal RCS stability of the transponders is comparable to the DBFT reflector, which has a more than 10-dB lower RCS. In Section IV-B, we show the implications of the RCS stability on the temporal phase stability.

3) Susceptibility to Systematic Temporal Variations: While the RCS of CRs typically does not show any dependency on temperature variation, it is important to know whether the RCS of transponders is susceptible to systematic temporal variations. The scatter plots in Fig. 8 show RCS time series of the transponders plotted against the hourly surface temperatures. The ascending tracks, i.e., the yellow triangles in Fig. 8, acquired in the afternoon, typically experience a higher temperature range over the seasons than the descending tracks.

The RCS variability of the units in the WASS test site does not show a significant correlation with temperature and neither do the descending data of the JABO test site. However, there is a significant correlation of −0.82 and −0.53 for the ascending data of the JABO test site, for units 141 and 148, respectively. This temperature dependency is observed: 1) in only one of the two test sites (JABO); 2) in only one of the two viewing geometries (ascending); 3) for environmental temperatures higher than 20 °C, which only occurs in the
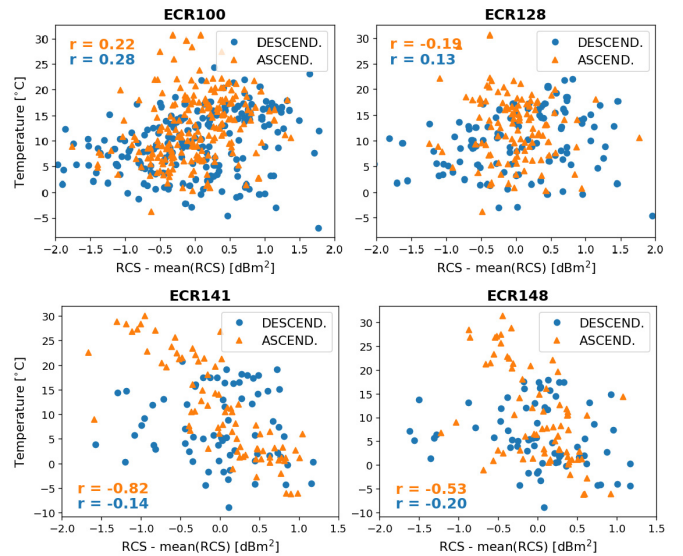

Fig. 8. RCS variability versus surface temperature for the four transponders, including Pearson's sample correlation coefficient *r*. Reduction by mean is performed per track.

ascending (afternoon) orbits; and 4) in two independent units (141 and 148). This suggests that temperature variations do not necessarily affect the RCS, but if they do, it occurs mainly for temperatures higher than 20 °C. In those cases, an increase in temperature results in a (slight) decrease of RCS for these acquisitions. Note that this would lead to a 1-dBm^2 reduction in RCS and, hence, a 1-dB reduction in SCR, which is equivalent to less than 0.2° phase error for an SCR > 30 dB.

B. InSAR Phase Stability

Deploying compact transponders is arguably most interesting for applications that use the phase information, i.e., SAR interferometry. This requires an assessment of the reliability and stability of the transponder phase. At the WASS test site,

TABLE VI
RCS STDs FOR CRs AND TRANSPONDERS IN dBm^2

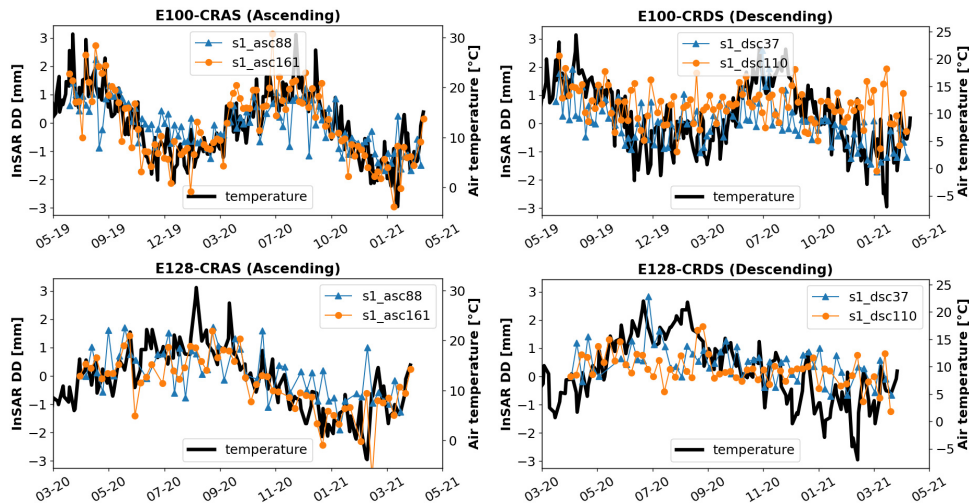| Target	Type	Site	average RCS	σ_{RCS}			
				ASC88	ASC161	DSC37	DSC110
CRAS / CRDS	reflector	WASS	39.0	.13	.19	.14	.19
DBFX	reflector	WASS	35.4	.24	.21	.16	.22
DBFT	reflector	WASS	28.6	.44	.42	.47	.44
100	transponder	WASS	38.4	.58	.68	.46	.46
128	transponder	WASS	42.4	.69	.68	.51	.30
141	transponder	JABO	43.9	.42	.63	.58	.40
148	transponder	JABO	43.4	.25	.62	.35	.36

Fig. 9. InSAR phase double-differences for units 100 and 128, relative to a reference corner reflectors, plotted against temperature for test site WASS.

we evaluate this using a configuration that combines transponders and CRs at distances of less than 70 m, which results in an atmospheric differential signal that is maximally 0.1 mm in the most extreme situations, but on average 0.03 mm [22], corresponding to 1.3° and 0.4° for C-band. This allows us to evaluate the temporal coherence, i.e., the phase stability, of the transponders, as the phase variance should be dominated by the clutter, described by the SCR of the transponders, and the sensor's thermal noise.

Flattened and topography-corrected interferograms were computed for all Sentinel-1 stacks, and subsequently, interferometric phase time series, evaluated at the IRF peaks, were used to compute double-differences phase time series between transponders and reflectors. Fig. 9 shows the DD phase time series between a transponder and a reference reflector, both for the ascending and the descending oriented antennas, for all Sentinel-1 tracks. As the seasonal signal is apparent in the time series, we also plot the surface temperature readings of the nearest meteostation (Voorschoten) obtained at the whole hour closest to the Sentinel-1 acquisition.

To verify that this signal is not coming from the reference reflectors, we also compute the DD time series between the independent reference reflectors (see Fig. 10). Since the seasonal signal is not visible for this baseline, we can attribute the temporal variability in Fig. 9 uniquely to the transponders. Likewise, scatter plots of the LOS displacement against temperature, see Fig. 11, from the ascending tracks, show a

significant correlation for the transponders and practically no correlation for CRs. The results from repeated leveling measurements between the concrete slabs carrying the reflectors exclude an actual displacement as a potential cause of the seasonal signal. Therefore, the phase measurements of the transponders are indeed sensitive to the temperature variations, with a typical dependency of 0.07–0.15 mm/°C. This phase sensitivity to temperature was also observed for other compact transponder prototypes in [23], with a correlation coefficient of 0.8.

For the transponders at test site JABO, we cannot compute independent phase DD as there is no nearby reference CR. Therefore, Fig. 12 only shows phase DD, converted to LOS displacements, over the very short baseline between units 141 and 148. Assuming the same temperature dependency for both the units, it should cancel out over this baseline. However, a residual correlation of the InSAR phases with the surface temperature is apparent. Unfortunately, in this case, we cannot rule out actual subsidence or uplift of one of the concrete blocks carrying the transponders.

In Fig. 12, we also compare the LOS displacement time series with the precipitation and snow cover data of test site JABO. The highest displacement gradient aligns with the time of the highest cumulative precipitation in September 2020. The sudden 2-mm phase jumps in January and February 2021 are clearly a consequence of the snow and ice cover on the
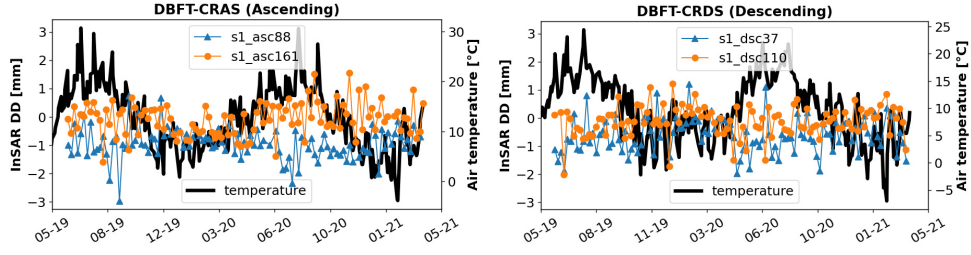
Fig. 10. InSAR phase DDs for two reference CRs, plotted against air temperature for test site WASS.
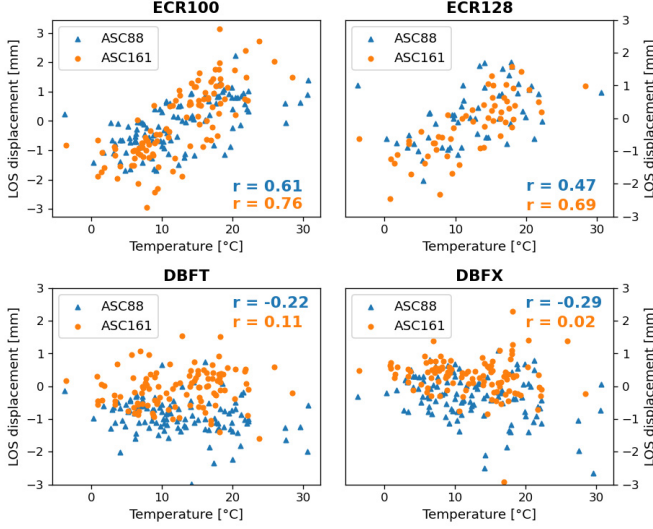

Fig. 11. InSAR LOS displacement of transponders (units 100 and 128) and reflectors (DBFT and DBFX) plotted against temperature for test site WASS.
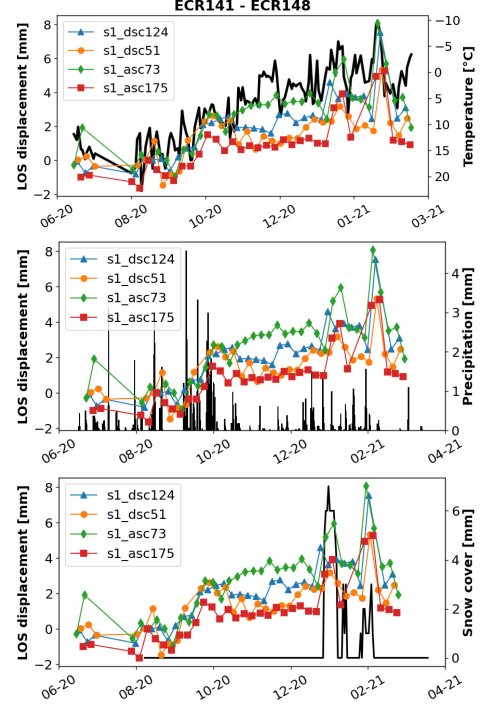

Fig. 12. Time series of InSAR phase double-differences (LOS displacement) between units 141 and 148, and surface temperature, precipitation, and snow cover for test site JABO.

transponder's radomes, as shown by the snow cover time series in Fig. 12.

To compensate for the influence of temperature on phase, the transponders would need to have an active temperature control system, such as used by calibration transponders [24]. This would, however, increase the complexity, energy consumption, and consequently the cost of the transponders.

Instead, we find that secular and seasonal effects in the time series can be effectively modeled in the postprocessing, as long as they remain trend stationary. Our results show that rather than using a universal correction, each individual transponder requires unique modeling. For each track, we estimate and remove the (seasonal) temperature-dependent signal from the InSAR DD time series $\Delta\phi_t$ for epochs $t \in (t_1; t_N)$, assuming the functional model

$$\mathbb{E}\left\{\begin{bmatrix} \Delta\phi_{t_1} \\ \Delta\phi_{t_2} \\ \vdots \\ \Delta\phi_{t_N} \end{bmatrix}\right\} = -\frac{4\pi}{\lambda}\begin{bmatrix} 1 & T_{t_1} \\ 1 & T_{t_2} \\ \vdots & \vdots \\ 1 & T_{t_N} \end{bmatrix}\begin{bmatrix} C \\ K_T \end{bmatrix} \quad (3)$$

where C is the constant offset, T is the measured temperature, and K_T is the temperature-dependent scaling factor. The time-dependent trend (drift) was not parameterized in (3), as no displacement trend is observed from the leveling measurements. However, we estimate the drift from the residuals and test its significance using the parameter significance test [25].

The estimated drift values are reported in Table VII. For unit 100, in track 88a and 37d, the estimated drifts are significant (level of significance $\alpha = 0.01$), while neither of the estimated drifts of unit 128 could be proven significant. Since the estimated residual drifts over the baseline between the CRs are not significant (see Fig. 10), we reject the hypothesis that reference reflectors have an influence on the observed drift of the transponders. Longer time series would be needed to obtain a more reliable estimate of the phase drift. Nonetheless, we can safely state that it is smaller than 1 mm per year.

After removing the estimated temperature-dependent signal and the residual drift, we assume that the phase residuals are representative of the phase noise and compute the STD of the residuals. Table VII shows the estimated STDs for the transponder–reflector (T/R), reflector–reflector (R/R), and transponder–transponder (T/T) baselines before ("raw") and after the trend removal ("detrended"). We compare the estimated STD with the STD predicted using the normalized amplitude dispersion (NAD) [26] and the temporal average SCR [21]. For the reflectors CRAS and CRDS, we have a

TABLE VII

InSAR Double-Difference Phase Standard Deviation and Drift, for Transponders 100, 128, 141, and 148, and for Reflectors CRAS, CRDS, DBFT, and DBFX. Abbreviation Detr. Stands for Detrended

Baseline	Track	InSAR DD phase STD [mm]				Residual drift [mm/yr]
		predicted		observed		
		SCR	NAD	raw	detr.	$\pm 1\sigma$
100–CRAS	88a	.2	.5	.8	**.5**	-0.5 ± 0.1
	161a	.2	.4	1.2	**.6**	-0.3 ± 0.2
–CRDS	37d	.2	.6	.8	**.6**	-0.4 ± 0.1
	110d	.2	.6	.7	**.6**	-0.3 ± 0.1
128–CRAS	88a	.2	.3	.9	**.7**	-0.7 ± 0.4
	161a	.2	.5	1.0	**.7**	-0.6 ± 0.3
–CRDS	37d	.2	.6	.6	**.6**	-0.4 ± 0.3
	110d	.2	.6	.5	**.5**	-0.6 ± 0.3
DBFT–CRAS	88a	.4	.4	.5	**.5**	-0.2 ± 0.1
	161a	.4	.4	.6	**.6**	$+0.2 \pm 0.1$
–CRDS	37d	.5	.5	.6	**.6**	0.0 ± 0.1
	110d	.4	.5	.5	**.5**	0.0 ± 0.1
DBFX–CRAS	88a	.3	.3	.5	**.5**	0.0 ± 0.1
	161a	.3	.3	.6	**.6**	0.0 ± 0.1
– CRDS	37d	.3	.3	.5	**.5**	-0.3 ± 0.1
	110d	.3	.3	.5	**.5**	-0.1 ± 0.1
141–148	73a	.1	.3	1.7	**.8**	$+0.9 \pm 0.8$
	175a	.1	.3	1.3	**.9**	$+1.0 \pm 0.9$
	51d	.1	.3	1.9	**1.1**	$+0.9 \pm 1.1$
	124d	.1	.3	1.6	**1.0**	$+1.1 \pm 1.0$

reliable estimate of their long-term phase STD. Their undifferenced single-epoch phase STD is $\sigma_{\psi_{CR}} = 0.11$ mm [19]. Therefore, an estimate of the DD phase STD for a T/R baseline is obtained by error propagation (assuming uncorrelated measurements) as

$$\sigma_{\Delta\phi_{T/R}} = \left(2\sigma_{\psi_R}^2 + 2\sigma_{\psi_T}^2\right)^{1/2} \qquad (4)$$

where σ_{ψ_T} is computed either from NAD or SCR. Table VII shows that the SCR-based estimation of the phase STD gives overly optimistic values. As the clutter of the transponders has not changed over the monitored period, the assumption of temporal ergodicity fails for the time series of the transponders' peak responses. In other words, the RCS variations are fully displayed in the phase instability. Therefore, the NAD provides a better STD proxy for the transponders.

Removing the trend and seasonal components lowers the STDs, cf. Table VII, where the most notable improvement is observed for the ascending tracks, which are more affected by temperature variations. For T/R baselines with units 100 and 128, we observe an average STD of 0.6 mm across all Sentinel-1 tracks. For T/T baseline 141–148, at test site JABO, the phase shifts caused by the temporary snow/ice cover increase the estimated phase STD up to 1.1 mm. The STDs of the undifferenced single-epoch phase measurements of the transponders (σ_{ψ_T} in (4)) vary between 0.3 and 0.8 mm.

C. Absolute Positioning

The positions of the transponder's antenna phase centers (PCs; both ascending and descending) in a terrestrial reference
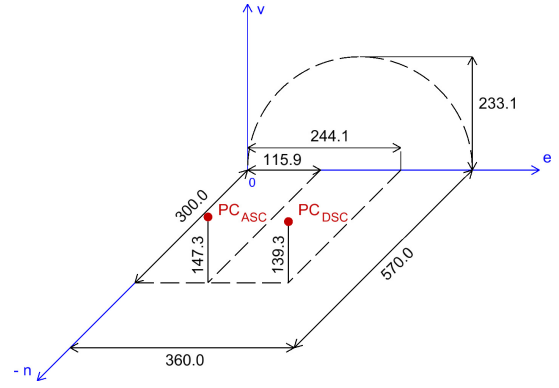

Fig. 13. Transponder dimensions and local topocentric offsets for ascending/descending antennas' phase centers in millimeters.
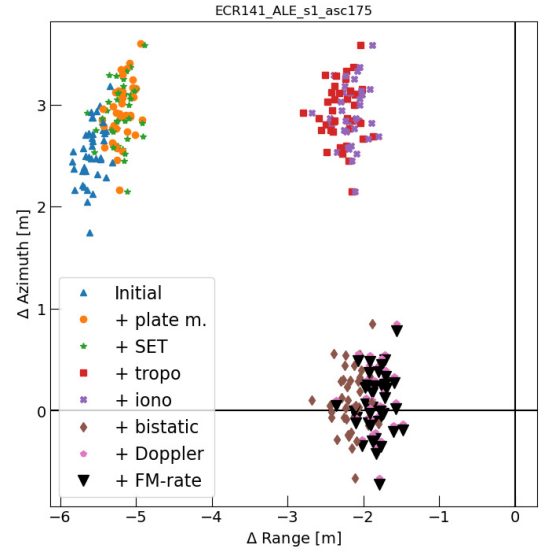

Fig. 14. Absolute positioning errors of transponder 141 from ascending track.

frame (TRF) were determined by applying a two-step procedure. First, we determined the coordinates of the transponder reference point, i.e., the northwestern corner of the base plate, see Fig. 13, using GNSS. For the JABO test site, we used static GNSS observations for 1 h (with a geodetic-grade receiver Trimble R10), connected to the ETRS89 coordinate reference system (ETRF2000 reference frame) via the nearby permanent reference station JABO (SKPOS network). For the WASS test site, we used four 90-s GNSS RTK observations (with a geodetic-grade receiver Trimble R8), connected to the ETRS89 coordinate reference system (ETRF2000 reference frame) using the NETPOS processing service of the Dutch Kadaster. Second, we computed the phase center coordinates, for each of the antennas, from the reference point coordinates using local coordinate offsets supplied by the manufacturer (see Fig. 13).

The accuracy (repeatability) of the TRF coordinates is 1–2 cm in the horizontal and 3 cm in the vertical direction. Orbit state vectors of Sentinel-1 satellites are given in the ITRF2014 reference frame with a sampling rate of 10 s, determined by the onboard GNSS receiver.

Absolute positioning errors (APEs) are epochwise differences between the detected subpixel peak coordinates and
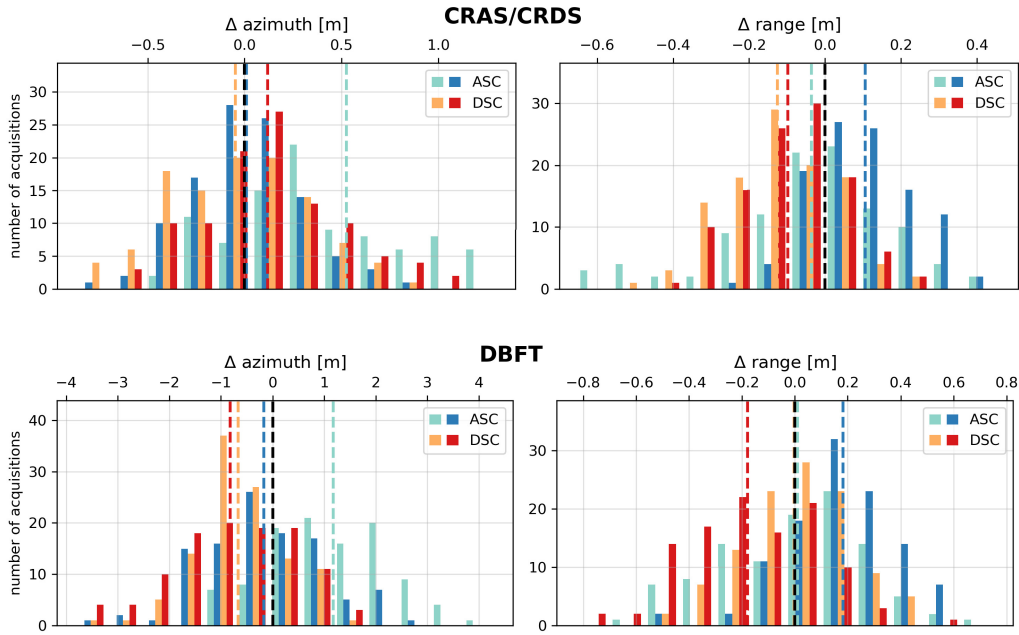
Fig. 15. Absolute positioning errors of the reference CRs at test site WASS.

the expected radar coordinates computed from the precise TRF positions via the inverse range-Doppler equations [27], correcting for all SAR timing biases. The APE in range (rg) and azimuth (az) is computed as

$$\mathrm{APE_{rg}} = \left(\tau_{\mathrm{peak,\ IPF}} - \tau_{\mathrm{predicted}}\right) \cdot c$$
$$\mathrm{APE_{az}} = \left(t_{\mathrm{peak,\ IPF}} - t_{\mathrm{predicted}}\right) \cdot v_{\mathrm{zeroDoppler}} \qquad (5)$$

where $v_{\mathrm{zeroDoppler}}$ is the satellite's ground-track zero-Doppler velocity. $\tau_{\mathrm{peak,\ IPF}}$ and $t_{\mathrm{peak,\ IPF}}$ are the azimuth and range time, respectively, of the subpixel peak positions in the SLC images as processed by the Sentinel-1's instrument processing facility (IPF). Predicted timings, $\tau_{\mathrm{predicted}}$ and $t_{\mathrm{predicted}}$, are composed of individual timing biases, i.e.,

$$\tau_{\mathrm{predicted}} = \tau_{\mathrm{ITRF}} + \Delta\tau_{\mathrm{SET}} + \Delta\tau_{\mathrm{tropo}} + \Delta\tau_{\mathrm{iono}} + \Delta\tau_{\mathrm{Doppler}}$$
$$t_{\mathrm{predicted}} = t_{\mathrm{ITRF}} + \Delta t_{\mathrm{SET}} + \Delta t_{\mathrm{bistatic}} + \Delta t_{\mathrm{FM\text{-}rate}} \qquad (6)$$

where the following holds.

1) *ITRF* represents positions directly obtained solving the range-Doppler equations from GNSS-determined coordinates in ITRS (ITRF2014 reference frame) at the particular acquisition epoch. The initial coordinates in ETRS89 (ETRF2000 reference frame) are first transformed to ITRS at the particular acquisition epoch, hence reflecting the plate motion.
2) *SET* represents timing corrections computed from topocentric solid Earth tides displacements, hence transforming from a "tide free" position (ITRF) to the instantaneous position as seen by the satellite (adding a permanent "mean tide," as well as a periodic components of tidal displacement using IERS SET displacement models [8]).
3) *Tropo* is the range timing correction for the slant tropospheric signal delay (modeled using the ECMWF ERA5 model [28]).

4) *Iono* is the range timing correction for the slant ionospheric signal delay (modeled using the CODE IGS global ionospheric model [29]).
5) *Bistatic* is the residual bistatic correction of the Sentinel-1 IPF in the azimuth timing [14].
6) *Doppler* are Doppler-centroid-induced range timing corrections [14].
7) *FM* represents the FM-rate mismatch of Sentinel-1 IPF in the azimuth timing [14].

Fig. 14 shows these corrections for transponder 141. Individual points in the figure represent epochwise SLC measurements. To verify the accuracy of the established APE computation framework, we compute the APE time series for the four reference reflectors at test site WASS (see Fig. 15). The observed APE and its temporal variance are limited by the Cramer–Rao lower bound (CRB) of the peak variance, determined by the reflector's SCR and the azimuth/range SLC resolutions [30]. The accuracy of the GNSS-determined TRF coordinates is 1–2 cm in the horizontal and 3 cm in the vertical direction. The Sentinel-1 orbital state vectors have a 3-D root-mean-square (rms) error of 5 cm [31]. According to the cross validation of the independently generated orbit solutions by [31], an orbit accuracy of ∼3 cm can be assumed. Considering the limited spatiotemporal resolution of the ERA5 model used for tropospheric delay correction and considering the RMS values of the total electron content maps of CODE ionospheric models, both tropospheric and ionospheric delay corrections could be assumed to exhibit an accuracy of ∼10 cm [22].

Using simple error propagation, these effects contribute to an overall prediction uncertainty (repeatability) of ∼11 cm in range and ∼4 cm in azimuth. The average SCR of reflectors CRAS and CRDS varies between 28 and 32 dB and yields a CRB of 28 and 4 cm in the azimuth and range directions, respectively. For these CRs, we achieve an average
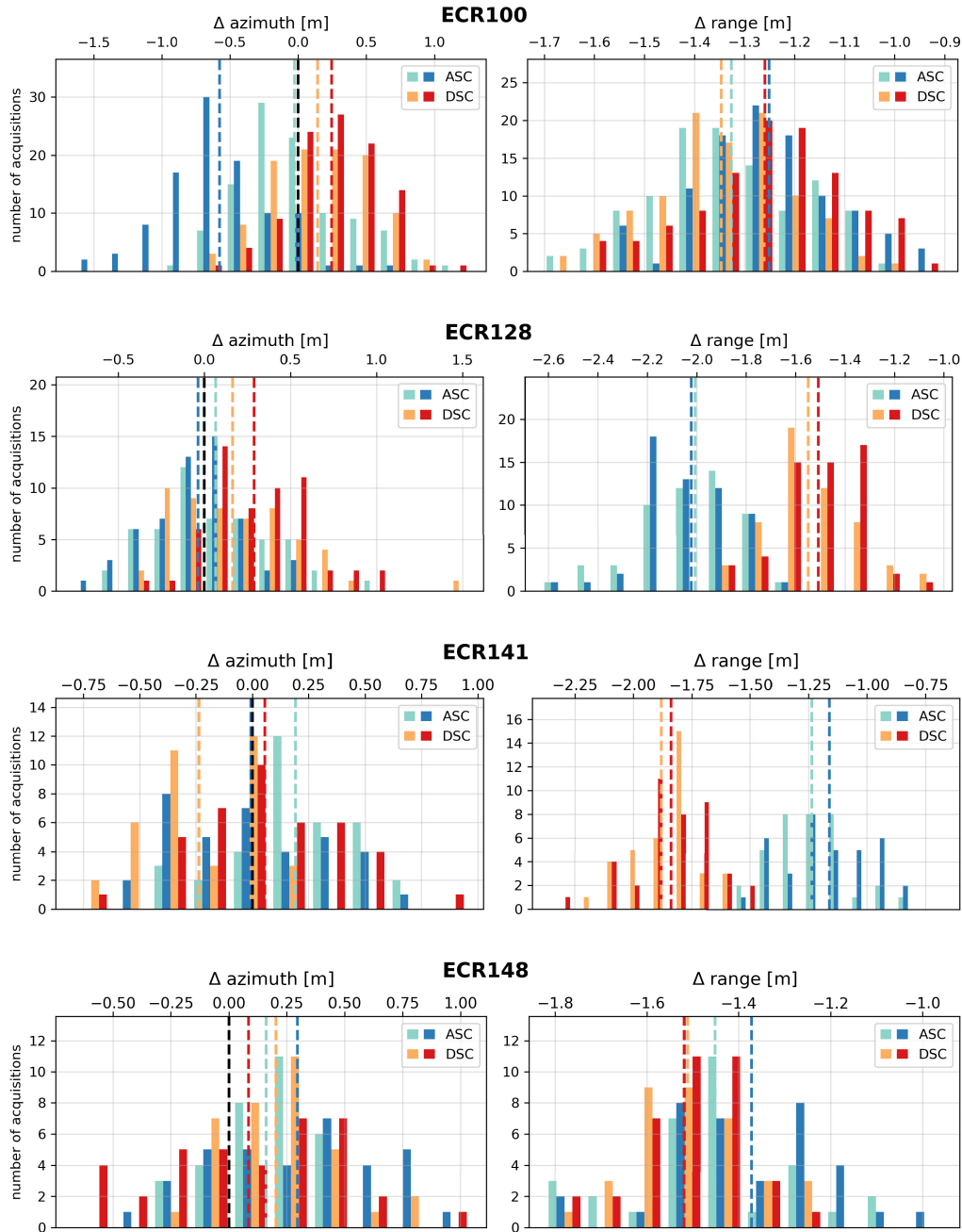
Fig. 16. Absolute positioning errors of the transponders from Sentinel-1 tracks.

STD of 42 and 13 cm in the azimuth and range directions, respectively. For Sentinel-1 IW products, Gisinger *et al.* [14] reported an achievable STD limit of 49.2 and 8.3 cm for azimuth and range, respectively, given 1.5-m triangular trihedral reflectors. Therefore, we consider our APE computation framework sufficient for precise APE analysis of the transponders.

Here, the absolute SAR positioning accuracy of the transponders is evaluated. In Table VIII, the average observed APE and its temporal STD are reported.

Fig. 16 shows the histograms of APE time series for the tested transponders. Observed systematic differences in the range coordinate are primarily caused by the internal

electronic delay of the transponders. An approximate internal electronic delay of $\sim$1.5 m (10×10^{-9} s), including the antennas and protective radome, was estimated in [5]. However, the observed average range differences vary between -1.24 and -2.10 m. Moreover, different internal delays are observed across the individual transponders and between ascending and descending tracks (see Fig. 17). Fig. 18 shows the average range delays plotted against the antenna misalignment in elevation and azimuth angles. We observe nonsystematic shifts between individual transponders. We also observe an apparent shift between ascending (negative $\Delta\alpha$) and descending (positive $\Delta\alpha$) tracks, which is highest for transponder 141 ($>$0.5 m) and smallest for transponder 148

TABLE VIII
APEs OF THE TESTED TRANSPONDERS ON SENTINEL-1 TIME SERIES

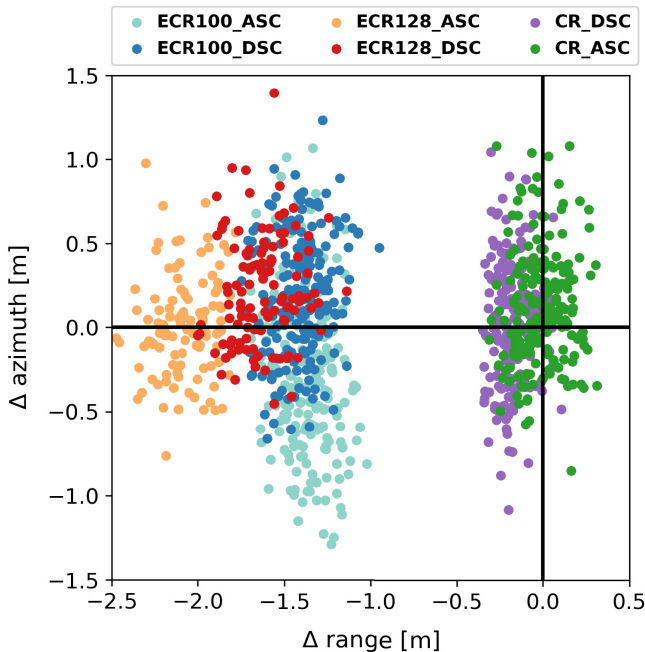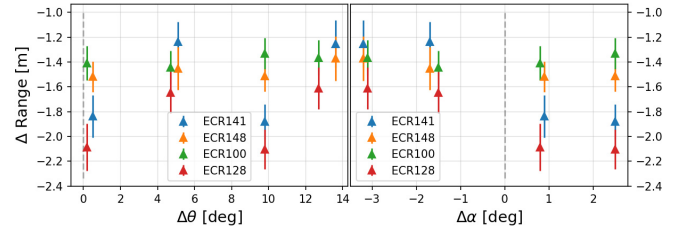| Transponder	Track	APE $\pm 1\sigma$ [cm]			
		azimuth		range	
100	88a	14.0	$\pm$ 36.6	-144.3	$\pm$ 13.5
	161a	24.2	$\pm$ 32.7	-136.5	$\pm$ 14.1
	37d	-57.8	$\pm$ 39.7	-133.3	$\pm$ 12.5
	110d	-2.0	$\pm$ 39.1	-140.9	$\pm$ 13.9
128	88a	16.4	$\pm$ 35.2	-164.7	$\pm$ 16.8
	161a	28.8	$\pm$ 27.9	-161.2	$\pm$ 16.9
	37d	-3.5	$\pm$ 26.5	-210.4	$\pm$ 16.1
	110d	6.7	$\pm$ 33.3	-208.7	$\pm$ 18.8
141	88a	19.2	$\pm$ 26.3	-123.6	$\pm$ 15.8
	161a	-0.6	$\pm$ 33.7	-125.3	$\pm$ 19.0
	37d	-23.7	$\pm$ 25.7	-188.0	$\pm$ 14.0
	110d	5.6	$\pm$ 30.1	-183.8	$\pm$ 17.2
148	88a	16.1	$\pm$ 20.8	-145.2	$\pm$ 17.3
	161a	29.7	$\pm$ 37.0	-137.2	$\pm$ 17.9
	37d	20.3	$\pm$ 24.1	-151.2	$\pm$ 12.6
	110d	8.5	$\pm$ 38.4	-151.9	$\pm$ 12.2

Fig. 17. Absolute positioning errors of the CRs (CRAS/CRDS) and the transponders 100/128 at the WASS test site using Sentinel-1 data.

Fig. 18. Internal range delay versus antennas misalignment in elevation ($\Delta\theta$) and azimuth ($\Delta\alpha$) angles. Error bars are 2.5σ.

V. CONCLUSION AND DISCUSSION

From the experimental results with four compact transponders manufactured in [5], installed at two different test sites, we conclude that they have an average RCS of 40–45 dBm^2, which is comparable to a triangular trihedral CR with a leg length of 2.0 m.

An antenna misalignment by 12° and 3° in elevation and azimuth angles, respectively (extreme values for Sentinel-1 over European latitudes), yields an RCS attenuation of up to 3 dB. While this attenuation is rather modest, by modifying the default antenna alignment for the site-specific viewing geometry, this attenuation can be further reduced. The temporal STD of the transponders' RCS is up to 0.7 dB, which is more than two times the STD observed for a CR of equivalent RCS, considering the 0.25-dB radiometric stability of the Sentinel-1 SLC measurements [32]. For some transponder units and sites with temperatures exceeding 20 °C, the RCS variability is correlated with temperature variations. We observed this only for ascending orbits on only one test site. As the RCS directly influences the SCR, which is often used as a proxy for the precision of the phase, we find that this approach yields a too optimistic precision estimate. The NAD gives a more realistic estimate of the phase precision.

Regarding the constant internal electronic delays, we find delays varying between 1.2 and 2.1 m. These are unit-specific and differ for ascending/descending antennas but could not be proven to be dependent on incidence angle or the azimuth of the zero-Doppler plane. Thus, for absolute centimeter-level geodetic positioning purposes, the transponders would require individual calibration models, similar as applied for geodetic GNSS antennas. The variable part of the absolute SAR positioning, in azimuth and range, is found to have a precision of 39.1 and 16.2 cm, respectively.

Regarding the precision of the double-difference interferometric phase, relative to a passive reference reflector, we observe a phase STD varying between 0.5 and 1.2 mm, which implies a single-epoch undifferenced STD of the transponder phase of 0.3–0.8 mm.

Yet, we observe the phase to be significantly correlated with environmental temperature variations, showing variations within a range of 6 mm. These can be modeled using a simple scaling factor that needs to be computed specific per transponder unit.

Estimating this temperature-dependent scaling factor, i.e., removing the seasonal variability, yields an observed InSAR phase STD of 0.5–0.7 mm in the LOS direction.

Regarding a potential phase drift, giving the maximum time interval of 21 months analyzed in this study, we find that

(<0.1 m). Although Gruber *et al.* [1] reported an incidence angle dependence of the transponder's internal range delay, our results could not confirm this. It is interesting to note the completely different range delay behavior between units 141 and 148, despite that these are separated only 46.5 m. For STDs of the range coordinate differences, even if the uncertainties of GNSS measurements, orbit state vectors, and atmospheric signal delay corrections are considered, we still reach at least a factor 2 worse results. The average azimuth coordinate differences are all within the confidence interval of their STDs. For azimuth STDs, we reach the limit dictated by the SCR (CRB) and the azimuth resolution ($\sim$22 m). More optimistic values are likely the result of the biased SCR estimate (see Section IV-A).

if apparent at all, it is less than 1 mm/y. This is especially important for long-term InSAR reliability.

Finally, snow or ice cover on the transponder radome may cause undesired phase spikes with larger magnitudes than the phase accuracy.

In general, based on our analysis of amplitude and phase, we observe that transponder units cannot be regarded as being equal. In fact, different units are specific in terms of their radiometric, geometric, and phase stability. This supports the suggestion of performing unit-specific calibrations, both by the manufacturer and considering site-specific conditions.

VI. PRACTICAL RECOMMENDATIONS

The decision of whether to deploy transponders is very dependent on the specific case study. Yet, there are a few general considerations that can be recommended for each application. First, estimating the clutter at the location of preferred deployment is strongly recommended. The clutter power should be preferably less than 4 dB, to obtain valuable estimates of phase, e.g., with an STD of better than 2 mm, and a distinct amplitude response. Second, when transponder units are ordered, the antenna orientation needs to be optimized for the specific geographic location of deployment. Note that this is not only latitude dependent, but it can also be optimized for the specific satellite orbits of interest. For example, for applications that require more (or less) sensitivity to vertical or horizontal displacement components, this is a parameter that can be optimized. Third, the transponders ideally need to include a calibration report with specific information on the constant and temperature-dependent internal delays. Alternatively, an on-site calibration campaign may be required, where we recommend to compute baselines with permanently installed CRs of sufficient size and with a well-known temporal behavior. Calibration activities containing two transponder units may not be sensitive to correlated signals, such as temperature variability. The duration of the calibration depends on the specific application. Several cross-track acquisitions are already sufficient to obtain a reasonable estimate of the RCS and the internal delay.

For further research, we recommend extending experiments using longer Sentinel-1 and Radarsat-2 SAR time series to further improve robust estimates on the InSAR phase stability, especially on the possible secular drift.

Finally, we strongly support international activities in permanent deployment of transponders, mechanically coupled to GNSS antenna infrastructure and tide gauges.

ACKNOWLEDGMENT

REFERENCES

[1] T. Gruber et al., "Geodetic SAR for height system unification and sea level research—Observation concept and preliminary results in the Baltic Sea," Remote Sens., vol. 12, no. 22, p. 3747, Nov. 2020.

[2] C. Gisinger et al., "First experiences with active C-band radar reflectors and Sentinel-1," in Proc. IEEE Int. Geosci. Remote Sens. Symp. (IGARSS), Sep. 2020, pp. 1165–1168.

[3] P. S. Mahapatra, S. Samiei-Esfahany, H. van der Marel, and R. F. Hanssen, "On the use of transponders as coherent radar targets for SAR interferometry," IEEE Trans. Geosci. Remote Sens., vol. 52, no. 3, pp. 1869–1878, Mar. 2014.

[4] P. Mahapatra, H. V. D. Marel, F. van Leijen, S. Samiei-Esfahany, R. Klees, and R. Hanssen, "InSAR datum connection using GNSS-augmented radar transponders," J. Geodesy, vol. 92, no. 1, pp. 21–32, Jun. 2017.

[5] MetaSensing. (2021). Metasensing BV: Radar Solutions—Electronic Corner Reflector—C Band (ECR-C). [Online]. Available: https://www.geomatics.metasensing.com/ecr-c

[6] D. R. Brunfeldt and F. T. Ulaby, "Active reflector for radar calibration," IEEE Trans. Geosci. Remote Sens., vol. GRS-22, no. 2, pp. 165–169, Mar. 1984.

[7] A. Freeman, Y. Shen, and C. L. Werner, "Polarimetric SAR calibration experiment using active radar calibrators," IEEE Trans. Geosci. Remote Sens., vol. 28, no. 2, pp. 224–240, Mar. 1990.

[8] IERS. (2021). International Earth Rotation and Reference Systems Service. [Online]. Available: https://www.iers.org/

[9] GKU Slovakia. (2021). Geodetic and Cartographic Institute. [Online]. Available: https://www.geoportal.sk/sk/udaje/ortofotomozaika/

[10] R. Hanssen, "A radar retroreflector device and a method of preparing a radar retroreflector device," International Patent WO 2 018 236 215 A1, Jun. 21, 2017. [Online]. Available: https://patents.google.com/patent/WO2018236215A1/en

[11] R. Czikhardt, H. van der Marel, and J. Papco, "GECORIS: An open-source toolbox for analyzing time series of corner reflectors in InSAR geodesy," Remote Sens., vol. 13, no. 5, p. 926, Mar. 2021.

[12] U. Balss et al., "Survey protocol for geometric SAR sensor analysis," German Aerosp. Center (DLR), Tech. Univ. Munich (TUM), Remote Sens. Lab. (RSL), Univ. Zurich, Cologne, Germany, Tech. Rep. DLR-FRM4SAR-TN-200, Apr. 2018.

[13] U. Balss, C. Gisinger, and M. Eineder, "Measurements on the absolute 2-D and 3-D localization accuracy of TerraSAR-X," Remote Sens., vol. 10, no. 4, p. 656, Apr. 2018, doi: 10.3390/rs10040656.

[14] C. Gisinger et al., "In-depth verification of Sentinel-1 and TerraSAR-X geolocation accuracy using the Australian corner reflector array," IEEE Trans. Geosci. Remote Sens., vol. 59, no. 2, pp. 1154–1181, Feb. 2021.

[15] A. L. Gray, P. W. Vachon, C. E. Livingstone, and T. I. Lukowski, "Synthetic aperture radar calibration using reference reflectors," IEEE Trans. Geosci. Remote Sens., vol. 28, no. 3, pp. 374–383, May 1990.

[16] A. Freeman, "SAR calibration: An overview," IEEE Trans. Geosci. Remote Sens., vol. 30, no. 6, pp. 1107–1121, Nov. 1992.

[17] N. Miranda and P. J. Meadows, "Radiometric calibration of S-1 level-1 products generated by the S-1 IPF," Eur. Space Agency (ESA), Paris, France, Tech. Rep. ESA-EOPG-CSCOP-TN-0002, May 2015.

[18] R. Piantanida, N. Miranda, and G. Hajduch, "Thermal denoising of products generated by the S-1 IPF," MPC, London, U.K., Tech. Rep. MPC-0392, Nov. 2017.

[19] R. Czikhardt, H. van der Marel, F. J. van Leijen, and R. F. Hanssen, "Estimating Signal-to-Clutter ratio of InSAR corner reflectors from SAR time series," IEEE Geosci. Remote Sens. Lett., early access, Apr. 14, 2021, doi: 10.1109/LGRS.2021.3070045.

[20] C. Leys, C. Ley, O. Klein, P. Bernard, and L. Licata, "Detecting outliers: Do not use standard deviation around the mean, use absolute deviation around the median," J. Exp. Social Psychol., vol. 49, no. 4, pp. 764–766, 2013.

[21] P. Dheenathayalan, M. C. Cuenca, P. Hoogeboom, and R. F. Hanssen, "Small reflectors for ground motion monitoring with InSAR," IEEE Trans. Geosci. Remote Sens., vol. 55, no. 12, pp. 6703–6712, Dec. 2017.

[22] R. F. Hanssen, Radar Interferometry: Data Interpretation and Error Analysis, vol. 2. Dordrecht, The Netherlands: Springer, 2001.

[23] G. Luzi, P. F. Espín-López, F. Mira Pérez, O. Monserrat, and M. Crosetto, "A low-cost active reflector for interferometric monitoring based on Sentinel-1 SAR images," Sensors, vol. 21, no. 6, p. 2008, Mar. 2021.

[24] S. Raab, B. J. Doering, D. Rudolf, J. Reimann, and M. Schwerdt, "Analysis of an improved temperature management concept for SAR system calibration transponders," in Proc. 11th Eur. Conf. Synth. Aperture Radar (EUSAR), 2016, pp. 1–6.

[25] K.-R. Koch, Parameter Estimation and Hypothesis Testing in Linear Models, 2nd ed. New York, NY, USA: Springer-Verlag, 1999.

[26] A. Ferretti, C. Prati, and F. Rocca, "Permanent scatterers in SAR interferometry," IEEE Trans. Geosci. Remote Sens., vol. 39, no. 1, pp. 8–20, Jan. 2001.

[27] I. G. Cumming and F. H. Wong, *Digital Processing of Synthetic Aperture Radar Data: Algorithms and Implementation*, vol. 1. Norwood, MA, USA: Artech House, 2005.

[28] H. Hersbach and D. Dee. (2016). *Era5 Reanalysis is in Production, ECMWF Newsletter 147*. [Online]. Available: https://www.ecmwf.int/en/newsletter/147/news/era5-reanalysis-production

[29] IGS. (2021). *International GNSS Service*. [Online]. Available: http://www.igs.org/

[30] R. Bamler and M. Eineder, "Accuracy of differential shift estimation by correlation and split-bandwidth interferometry for wideband and delta-k SAR systems," *IEEE Geosci. Remote Sens. Lett.*, vol. 2, no. 2, pp. 151–155, Apr. 2005.

[31] H. Peter *et al.*, "Sentinel-1A—First precise orbit determination results," *Adv. Space Res.*, vol. 60, no. 5, pp. 879–892, Sep. 2017.

[32] *Sentinel-1A N-Cyclic Performance Report—2020–07*, Collecte Localisation Satell. (CLS), Ramonville Saint-Agne, France, Jul. 2020.

Juraj Papco received the Ph.D. degree in geodesy and cartography from the Slovak University of Technology, Bratislava, Slovakia, in 2010.

Since 2004, he has been a Researcher and a Lecturer in global geodesy and remote sensing with the Slovak University of Technology. As the principal investigator, he has experience in managing several satellite-interferometric synthetic aperture radar (InSAR)-related projects, unique for Slovakia territory. His main research interests include satellite geodesy, global navigation satellite systems (GNSS), remote sensing, SAR and InSAR, deformation monitoring, gravity field modeling, gravimetry, and land surveying.

Richard Czikhardt received the M.Sc. degree in geodesy and cartography and the Ph.D. degree from the Department of Theoretical Geodesy and Geoinformatics, Slovak University of Technology, Bratislava, Slovakia, in 2017 and 2021, respectively.

In 2019, he was a Research Intern at the Department of Geoscience and Remote Sensing, Delft University of Technology, Delft, The Netherlands. He has practical experience with interferometric synthetic aperture radar (InSAR) software development, time series analysis, image processing, satellite and ground-based geodetic techniques, and geographic information systems. His primary research is on InSAR geodesy, focusing on advanced InSAR processing techniques, quality control, and geodetic integration using artificial radar reflectors.
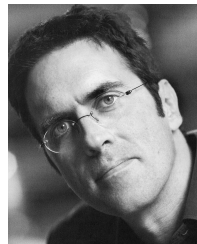
Hans van der Marel received the M.Sc. degree in geodetic engineering and the Ph.D. degree *(cum laude)* from the Delft University of Technology, Delft, The Netherlands, in 1983 and 1988, respectively.

From September 1983 until July 1987, he was a Research Fellow with The Netherlands Organisation for Scientific Research, The Hague, where he worked on the scientific data reduction for the astronomical satellite Hipparcos. From 1987 until 1989, he was a Research Fellow with the Netherlands Academy of Sciences, Amsterdam, The Netherlands. In 1989, he became an Assistant Professor in global navigation satellite systems (GNSS) at the Delft University of Technology, with a specific interest in high-precision scientific and meteorological applications of GNSS. He is currently an Assistant Professor with the Department of Geoscience and Remote Sensing, Delft University of Technology.

Ramon F. Hanssen (Senior Member, IEEE) received the M.Sc. degree in geodetic engineering and the Ph.D. degree *(cum laude)* in geodetic engineering from the Delft University of Technology, Delft, The Netherlands, in 1993 and 2001, respectively.

He was with the International Institute for Aerospace Survey and Earth Science; the University of Stuttgart, Stuttgart, Germany; the German Aerospace Center (DLR), Oberpfaffenhofen; Stanford University (Fulbright Fellow), Stanford, CA, USA; and the Scripps Institution of Oceanography, San Diego, CA, USA, where he worked on microwave remote sensing, radar interferometry, signal processing, and geophysical application development. Since 2008, he has been an Antoni van Leeuwenhoek Professor in geodesy and satellite Earth observation at the Delft University of Technology. He is the author of a textbook on radar interferometry.